Materials Science & Engineering A 766 (2019) 138353

Contents lists available at ScienceDirect

Materials Science & Engineering A

journal homepage: www.elsevier.com/locate/msea

Creep behavior of a 10%Cr heat-resistant martensitic steel with low nitrogen and high boron contents at 650 °C

N. Dudova*, R. Mishnev, R. Kaibyshev

Belgorod State University, Belgorod, 308015, Russia

ARTICLE INFO

Keywords:
Martensite
Steel
Creep
Electron microscopy
Precipitation
Coarsening

ABSTRACT

The purpose of this study is to identify the relationships between the creep behavior of the 10% Cr martensitic steel with 0.008% B and 0.003% N and changes in microstructure and precipitations of secondary phases. Creep tests were carried out at 650 °C under an applied stress ranging from 180 to 120 MPa. The 10% Cr steel exhibits a linear stress vs. time to rupture dependence without creep strength breakdown up to approximately 40 000 h. The 100 000 h creep rupture strength at 650 °C is predicted to be 110 MPa. The high creep strength of the 10% Cr steel is attributed to high threshold stress of 111.5 MPa. Threshold stress is associated with the detachment stress, i.e. the stress required for detachment of dislocations from $M_{23}C_6$ carbides after finishing the climb, mainly. Analysis of the pinning pressures exerted from different precipitates shows that $M_{23}C_6$ carbides also play the main role in preventing the lath boundary migration and therefore, provide high stability of the tempered martensite lath structure under creep conditions. Coarsening of the lath structure under long-term creep conditions is associated with growth of Laves phase particles, mainly.

1. Introduction

Power plants of new generations with ultrasupercritical (USC) and advanced ultrasupercritical (A-USC) steam parameters require heat-resistant materials with enhanced creep resistance at 650–720 °C [1–4]. Consequently, austenitic steels and nickel-based superalloys will be used for the most heated components [4]. Nevertheless, high-chromium (9–12% Cr) heat-resistant martensitic/ferritic steels will consist the main part of materials for fossil power plants due to their lower cost, smaller thermal expansion and larger thermal conductivity as compared with austenitic steels and nickel-based alloys, excellent combination of creep strength and fatigue resistance [5]. So, further improvement of their creep strength is required.

Microstructure of high-chromium martensitic steels is the complex structure composed of prior austenite grains, packets, blocks and laths with a high dislocation density in the lath interiors [1,2,4–14]. The dispersion strengthening of these steels is provided, mainly, by nanoscale boundary $M_{23}C_6$-type carbides and homogeneously distributed in the laths MX carbonitrides. This tempered martensite lath structure (TMLS) is considered to be the main determining factor for retaining the creep strength during long-term creep [6–14]. Transformation of the non-equilibrium lath structure into the subgrain structure occurs during long-term creep and leads to a quick degradation of the creep rupture strength. The alloying design and heat treatment of high-chromium steels are aimed to improve the stability of TMLS under creep conditions.

Different approaches are being taken to provide an optimal balance of solid-solution, dislocation, substructure, and dispersion strengthening of high-chromium steels. As known, varying the proportion of main dispersed phases such as $M_{23}C_6$, MX and Laves phase coexisted in the steels under creep condition affects the creep strength. $M_{23}C_6$ carbides located at boundaries act as obstacles to dislocation climb motion and slow down the recovery of TMLS [15]. MX carbonitrides prevent the dislocation motion in the lath interiors. MX phase can be classified into Nb- and C-rich and V- and N-rich particles, also Ti-rich particles are often distinguished [16–19]. Precipitation of fine V-rich particles may continue during creep test [16,19]. Both $M_{23}C_6$ carbides and MX carbonitrides slow down the knitting reaction between free dislocations and dislocations comprising low-angle interlath boundaries hindering their transformation to subgrain boundaries and relieving internal stress [20,21]. These particles also play the role of pinning agents, which impede migration of low-angle boundaries of laths/subgrains and high-angle boundaries under creep condition. The important role of $M_{23}C_6$ and MX particles in the creep resistance is obvious, however the strengthening mechanism of MX carbonitrides and optimal combination of $M_{23}C_6$ and MX phases in the high-chromium steels are the

* Corresponding author.
E-mail address: dudova@bsu.edu.ru (N. Dudova).

https://doi.org/10.1016/j.msea.2019.138353
Received 25 July 2019; Accepted 28 August 2019
Available online 29 August 2019
0921-5093/

Table 1
Structural parameters of the 10% Cr steel in tempered condition and after creep tests at 650 °C under different stresses.

		Initial state	180 MPa gauge/grip	160 MPa gauge/grip	140 MPa gauge/grip	120 MPa gauge/grip
Time, h		0	18.7	211	1426	39 437
Elongation, %		0	45.7	13.7	15.9	9.2
Lath width, nm		380	700/480	660/480	660/510	861/614
Dislocation density, $\times 10^{14}$ m^{-2}		1.7	1.2/1.7	0.95/1.7	1.0/1.1	0.20/0.43
Mean size of particles, nm	$M_{23}C_6$	70	70/65	80/74	100/89	120.4/96
	Laves phase	—	56/62	111/100	156/132	320/330
	Nb-rich MX	30	45/37	44/37	55/52	38.5/35
	V-rich MX	40 (negligible amount)	—/—	—/—	—/—	67/58
	M_6C	25	—/—	—/—	—/—	—/—
	Z-phase	—	—/—	—/—	—/—	120/—

subject to discussion of materials scientists.

One of the most advanced approaches to the microstructural design was suggested by the National Institute for Materials Science (NIMS), Japan. It is consisted in the increasing the B content to approximately 0.01 wt% and decreasing the N content to approximately thousandths of a percent in 9–11%Cr steels [3,22–24]. This approach results in an increase in the long-term creep resistance of the steels [14,19]. The high boron content provides the two-phase separation of $M_{23}C_6$ carbides to B-free $M_{23}C_6$ carbides and the $M_{23}(B{\cdot}C)_6$ phase and refinement of these particles to 70 nm [25–27]. The $M_{23}(B{\cdot}C)_6$ phase is highly resistant to coarsening as compared to the B-free $M_{23}C_6$ carbides, due to the decreased energy of $Fe_\alpha(110)\,||M_{23}(C{\cdot}B)_6(111)$ interfaces [26]. M_2B borides were revealed to affect the high stability of carbides [27]. Fine borides are formed at boundaries during normalizing and act as nucleation sites for B-rich carbides that can delay the carbide growth [27]. The lowering of the N content leads to a significant decrease in the volume fraction of V-rich MX carbonitrides and suppresses the formation of Z-phase (CrVN nitride) because carbon cannot replace nitrogen in this phase. So, in these steels with high B and low N contents the volume ratio of $M_{23}C_6$ and MX phases is significantly different as compared to conventional steels with usual N (0.05 wt%) and B (0.003 wt%) contents. Nevertheless, the lower fraction of MX particles does not prevent the achievement of higher creep resistance [19].

In this paper we investigate the creep behavior of the advanced 10% Cr steel and analyze the role of dispersed particles in high creep resistance of this steel.

2. Experimental procedure

A steel with the following chemical composition (in wt%) was examined: 0.1% C; 0.06% Si; 0.1% Mn; 10.0% Cr; 0.17% Ni; 0.7% Mo; 0.05% Nb; 0.2% V; 0.003% N; 0.008% B; 2.0% W; 3.0% Co; 0.002% Ti; 0.006% Cu; 0.01% Al and Fe balance. This material is herein denoted 10% Cr steel. The 10% Cr steel was solution treated at 1060 °C for 0.5 h, cooled in air, and subsequently tempered at 770 °C for 3 h. Flat specimens with a gauge length of 25 mm and cross-sectional dimensions of 7 mm × 3 mm were subjected to creep tests until rupture under an applied stress of 120, 130, 140, 160 and 180 MPa at 650 °C. Also some creep tests were carried out at temperatures of 600 and 620 °C under an applied stress ranging from 160 to 200 MPa. Tensile tests were carried out using flat specimens with a gauge length of 35 mm and cross-sectional dimensions of 7 mm × 3 mm using an Instron 5882 testing machine at temperature of 650°C and strain rates in the interval 10^{-3} -10^{-5} s^{-1}. Hardness was measured using the Wolpert 3000BLD device at room temperature.

Structural characterization was performed using a Jeol JEM-2100 transmission electron microscope (TEM) with an INCA energy dispersive X-ray spectrometer and using the Z-contrast technique with a Quanta 600FEG scanning electron microscope (SEM) equipped with an electron backscatter diffraction (EBSD) pattern analyzer incorporating an orientation imaging microscopy (OIM) system. Low- and high-angle boundaries (LABs and HABs) were defined to have a misorientation of $2^\circ < \theta \leq 15^\circ$ and $> 15^\circ$ and depicted in misorientation maps using white and black lines, respectively. Kernel average misorientation (KAM) value for each pixel is defined as the average misorientation that a pixel has with its 6 neighbors. The transverse lath/subgrain sizes were measured on the TEM micrographs by the linear intercept method, counting all the clear visible (sub)boundaries. The dislocation densities were estimated by counting the individual dislocations in the (sub) grain/lath interiors per unit area on at least six arbitrarily selected typical TEM images for each data point. The density of particles located at (sub)grain/interlath boundaries was determined as the number of particles per unit boundary length. Other details of structural characterization were reported in previous works [14,19,25].

The equilibrium volume fractions of phases were calculated by the version 5 of the Thermo-Calc software using the TCFE7 database by entering the BCC A2, FCC A1, M23C6 and LAVES PHASE C14 as equilibrium phases for the actual steel composition.

3. Results

3.1. Tempered martensite lath structure

The TMLS and secondary-phase particles in the 10% Cr steel in the tempered condition were described in previous works [14,19,25]. The main structural parameters are presented in Table 1. Under tempering, the structure is composed of a hierarchical sequence of prior austenite grains (PAGs) (mean size of 35 μm), packets, blocks, and laths (Fig. 1(a) and (b)). The mean lath width is about 0.4 μm, whereas the values of lath width vary from 100 nm to 1 μm (Fig. 1(b) and (c)).

The peculiarities of dispersed particles in the tempered 10%Cr steel as compared to conventional high-chromium steels with standard N and B contents consist in:

1) the smaller average size of $M_{23}C_6$ carbides of 70 nm (Fig. 1(b) and (d));
2) the higher volume fraction of $M_{23}C_6$ carbides (2.05% in contrast to 1.78% in the P92 steel [28]) and corresponding higher distribution density of particles on the lath/(sub)grain boundaries (2.18 μm^{-1} in contrast to 0.94 μm^{-1} in the P92 steel) [28];
3) MX particles are represented by Nb-enriched M(C,N) carbonitrides with average size of 30 nm whereas the fraction of V-rich M(C,N) particles is negligibly low after tempering.

3.2. Static mechanical properties

The mechanical properties of the 10% Cr steel at temperature of 650 °C are the following: the yield stress is 300 MPa, the ultimate tensile strength is 320 MPa, and the total elongation is 25.7% at strain rate of 2×10^{-3} s^{-1}. Hardness is 220 HB.

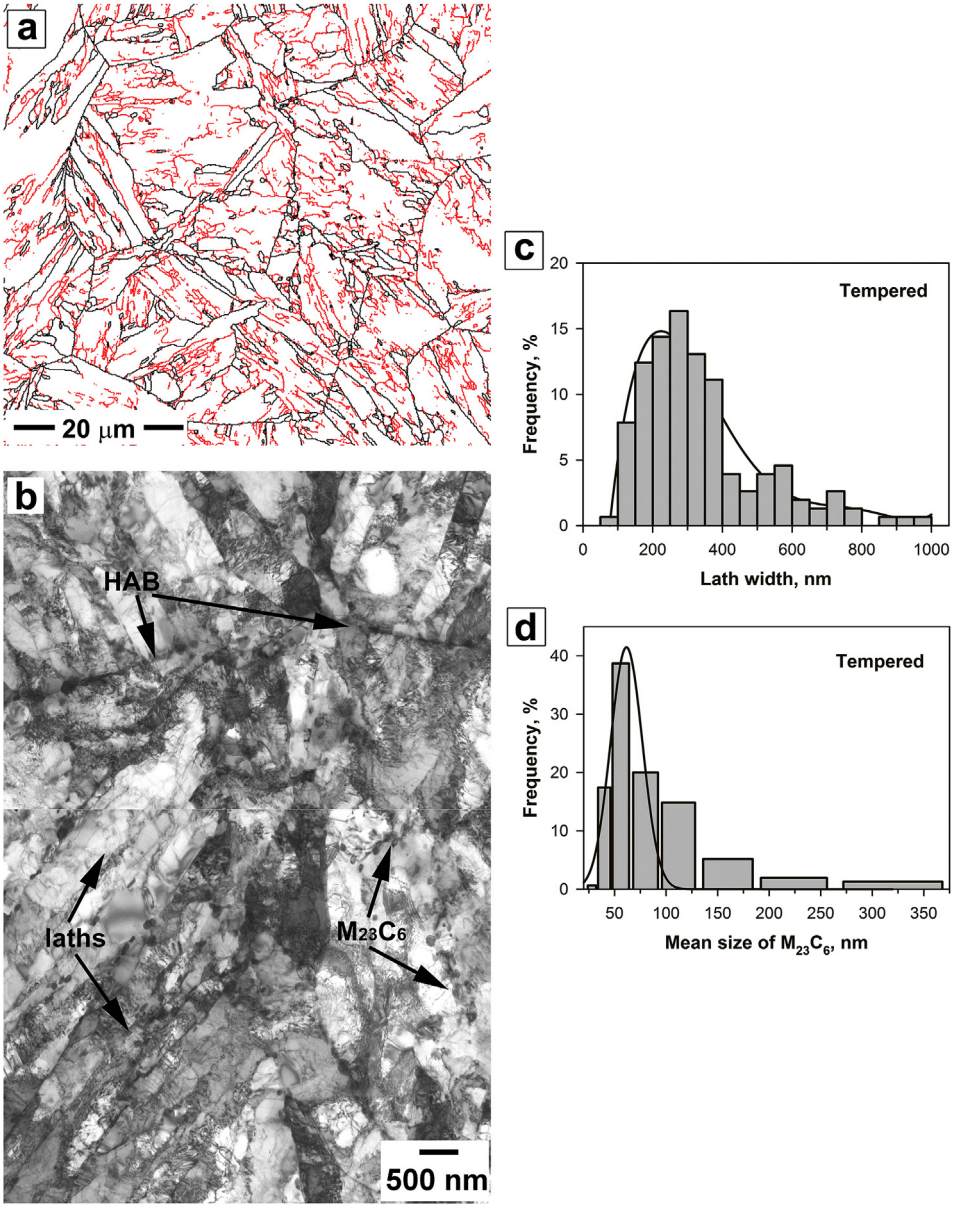

Fig. 1. Typical micrographs of the tempered 10% Cr steel: a) boundary map (black and red lines correspond to boundaries with misorientations of $\theta \geq 15^{\circ}$ and $2^{\circ} \leq \theta < 15^{\circ}$, respectively); b) TEM micrograph showing the laths structure and precipitated $M_{23}C_6$ carbides on boundaries. Distributions of lath width (c) and mean size of $M_{23}C_6$ carbides (d). (For interpretation of the references to colour in this figure legend, the reader is referred to the Web version of this article.)

3.3. Creep behavior

Creep rupture time of the 10% Cr steel depends linearly on the applied stress up to 120 MPa that corresponds to rupture time of 39 437 h at a temperature of 650 °C (Fig. 2(a)). Creep strength breakdown does not occur in the stress range studied in contrast to the conventional 9% Cr steels containing 0.05%N and 0.003%B [14]. Two creep regions can be distinguished on the stress-time curve despite its

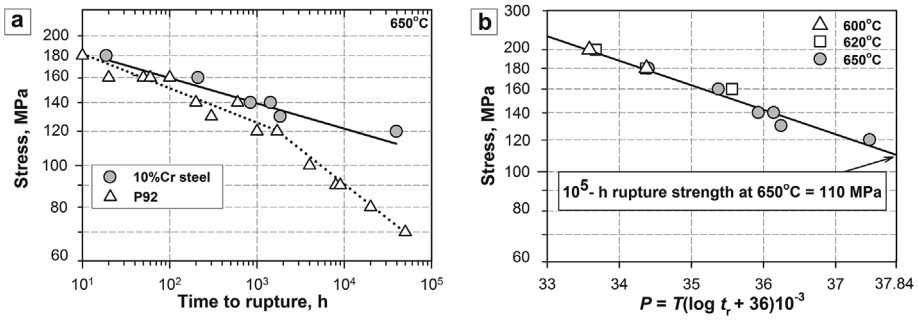

Fig. 2. Time to rupture vs. stress curve (a) at 650 °C for the 10%Cr steel in comparison with data for P92 steel [37] and Larson-Miller diagram (b).

Table 2
Creep tests results (time to rupture in hours) of the 10% Cr steel at different temperatures and stresses.

Applied stress, MPa	120	130	140	160	180	200
T, °C						
650	39 437	1840	1425	211	19	–
620	–	–	–	6653	308	51
600	–	–	–	–	2388	295

linear character: the short-term or high-stress region at 180-130 MPa with time to rupture less than 2000 h and the long-term or low-stress region at ≤ 120 MPa with time to rupture of about 40 000 h and more (Fig. 2(a)).

The long-term creep rupture strength for the rupture time of 10^5 h can be predicted using the Larson-Miller parameter [29]:

$$P = T\,(\log t_r + 36)\cdot 10^{-3} \quad (1)$$

where T is the absolute temperature, t_r is the time to rupture. Fig. 2(b) shows the applied stress vs. P graph constructed from experimental creep rupture data at temperatures of 600, 620 and 650 °C at different applied stresses ranging from 200 to 120 MPa (Table 2). The curve point at the right vertical axis corresponds to the predicted long-term creep rupture strength at 650 °C for 10^5 h, which is 110 MPa. This value is approximately 50% larger than for the P92 steel (72 MPa) [30] and approximately 30% larger than for the 3% Co-modified P92 steel (85 MPa) [31].

Neck formation of specimens during creep tends to decrease with decreasing the applied stress. The reduction in area of specimen after long-term creep test at 120 MPa comprises 22% that is 3 times lower than that of specimens after short-term creep test at 130–180 MPa (Fig. 3). High elongation of 45% was attained only at the highest applied stress of 180 MPa whereas at 130–160 MPa elongation decreases by a factor of 3.

The time and strain dependencies of the creep rate, $\dot{\varepsilon}$, at different stresses of the 10% Cr steel are shown in Fig. 4(a) and (b), respectively. In the short-term region (180-130 MPa), the minimum creep rate is reduced by approximately one order of magnitude with each decrease in the applied stress by 20 MPa. In contrast, more significant reduction by approximately 2 orders of magnitude occurs when applied stress decreases from 140 … 130 to 120 MPa (Fig. 4(a) and (b), Table 3).

The three stages can be distinguished on the creep curves (Fig. 4(b)). The transient creep strain, ε_T, the duration of apparent steady-state stage evaluated as creep strain accumulation at the minimum creep rate ($\dot{\varepsilon}_{min}\cdot t_r$, where t_r is the rupture time) and tertiary creep strain, ε_3, were estimated by using the technique described in

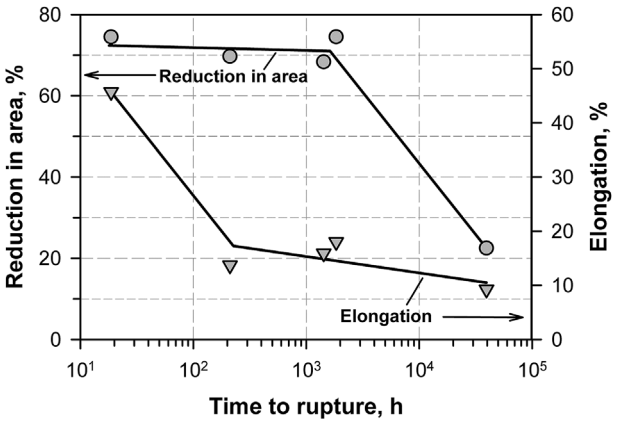

Fig. 3. Change in the reduction in area and elongation of the specimens creep tested at 650 °C with time to rupture.

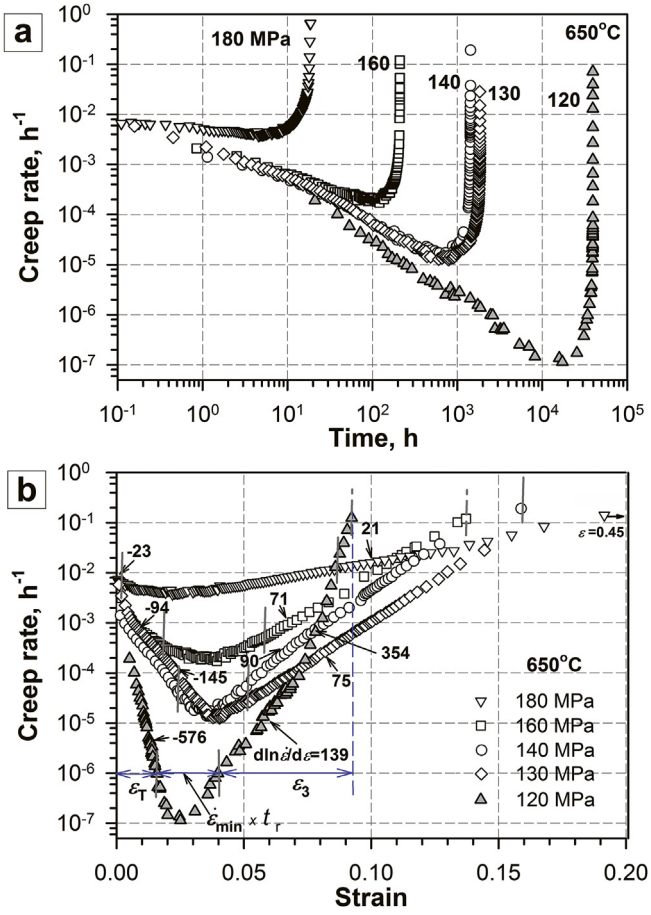

Fig. 4. Creep rate vs. time (a) and strain (b) curves at 650 °C and different applied stresses from 120 to 180 MPa.

Refs. [16,32,33].

Transient stage. The length of transient stage increases in the short-term region from the negligibly small value at 180 MPa to 2.8% at 130 MPa, whereas it decreases again to 1.6% in the long-term region at 120 MPa (Fig. 4(b), Table 3). Under transient creep, the decrease in the creep rate with time is characterized by the rate of exhaustion of transient creep, r', as evaluated using the following relationship, which was proposed by Garofalo [33]:

$$\varepsilon = \varepsilon_0 + \varepsilon_T[1 - \exp(-r'\cdot t)] + \dot{\varepsilon}_s\cdot t, \quad (2)$$

where ε is the strain, ε_0 is the instantaneous strain on loading, $\dot{\varepsilon}_s$ is the steady-state creep rate, which can be replaced by the $\dot{\varepsilon}_{min}$ value [33], and t is the time. The r' value was estimated graphically as the slope of the $\ln(1 - \Delta/\varepsilon_T)$ vs. time plot, where Δ is the transient creep component ($(\Delta = \varepsilon - \varepsilon_0 - \dot{\varepsilon}_{min}\cdot t_r)$ [33]. The rate of exhaustion of transient creep decreases with decreasing the creep rate/applied stress (Fig. 5, Table 3) that can be indicative of the slower processes of rearrangements of the lattice dislocations at the transient stage at lower stresses.

Apparent steady-state stage. The 10% Cr steel exhibits a minimum creep rate, $\dot{\varepsilon}_{min}$, instead of steady state that is typical for martensitic steels [1]. The decrease in the applied stress from 180 to 120 MPa leads to the following changes: 1) the length of the steady-state stage decreases from 8.8% at 180 MPa to 2.5% at 120 MPa that correlates with a decrease in the elongation; 2) the minimum creep rate decreases from approximately 10^{-3} to 10^{-7} h^{-1}; 3) the off-set strain, at which the minimum creep rate is attained, increases from 2.2% to 3.5 … 3.8% in the short-term region (180–140 … 130 MPa), whereas it decreases to 2.5% at 120 MPa (Fig. 4(b), Table 3).

Dependence between the minimum creep rate and applied stress

Table 3
Parameters of creep behavior of the 10% Cr steel during creep testing at 650 °C under different stresses from 120 to 180 MPa.

Applied stress, MPa	t_r, h	ε, %	$\dot{\varepsilon}_{min}$, s^{-1}	$\dot{\varepsilon}_{min}$, h^{-1}	ε_{min}, %	ε_T, %	$\dot{\varepsilon}_{min} \times t_r$, %	ε_3, %	r', h^{-1}	p, h^{-1}
120	39 437	9.2	3.2×10^{-11}	1.15×10^{-7}	2.5	1.58	2.52	5.20	0.000194	0.000151
130	1840	18.0	3.6×10^{-9}	1.3×10^{-5}	3.8	2.82	2.93	12.25	0.00708	0.004
140	1426	15.9	3.9×10^{-9}	1.4×10^{-5}	3.5	2.19	3.14	10.55	0.005	0.01
160	211	13.7	4.8×10^{-8}	1.9×10^{-4}	3.7	1.31	4.69	10.04	0.0297	0.0679
180	19	45.7	1.0×10^{-6}	3.7×10^{-3}	2.2	–	8.78	36.92	–	1.22

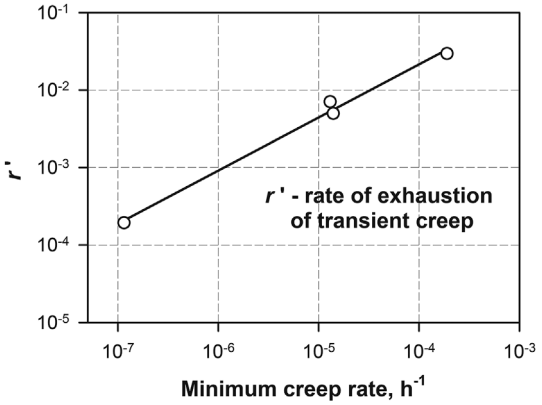

Fig. 5. Change in the parameter of r' with minimum creep rate.

obey a power law relationship [1,13,20,34,35]:

$$\dot{\varepsilon}_{min} = A\sigma^{n^*} \quad (3)$$

where A is a constant, σ is the stress, n^* is the apparent stress exponent. Fig. 6 shows the dependence of the minimum creep rate vs. stress as plotted on double logarithmic scale. The data at high stresses (> 200 MPa) were determined from the tensile tests with a different strain rate ranging from $\sim 10^{-5}$ to $\sim 10^{-3}$ s^{-1}. An apparent stress exponent $n^* = 23$, that is about two times larger than that for the conventional high-chromium P92-type steel [20,36–38] and 3% Co-modified P92 steel [13].

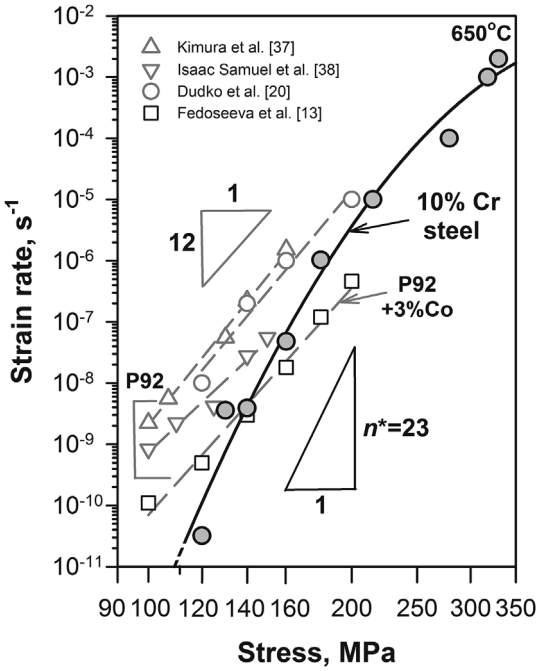

Fig. 6. Stress vs. minimum creep rate curve of the 10%Cr steel at 650 °C in comparison with data for the P92 steel [20,37,38] and 3%Co-modified P92 steel [13].

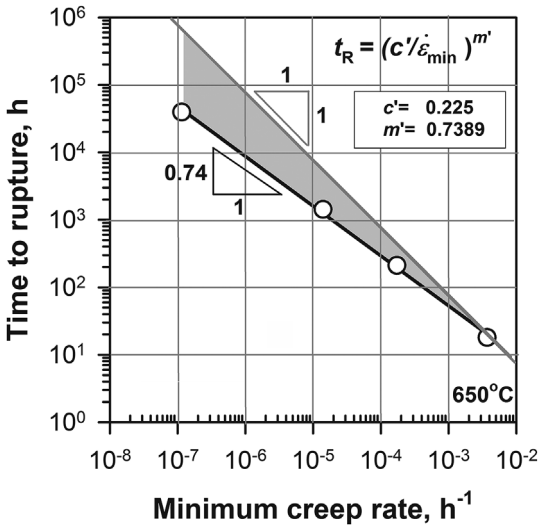

Fig. 7. Monkman - Grant relationship of the 10% Cr steel at 650 °C.

The time to rupture is inversely proportional to a decrease in the minimum creep rate as shown in the Monkman-Grant plot (Fig. 7) in accordance with the relationship [11,39]:

$$t_r = (c'/\dot{\varepsilon}_{min})^{m'} \quad (4)$$

where c' and m' are the constants. It is clearly seen that the Monkman-Grant relationship is linear in the studied stress range. However, experimental data deviate downward from the line with $m' = 1$ indicating $m' < 1$. This finding means that the 10 times decrease in the minimum creep rate does not lead to the 10-fold increase in the time to rupture. At 650 °C, the estimated coefficient c' is approximately 0.225 and m' is 0.74.

Tertiary creep. Creep behavior in the tertiary stage is significantly different in the short-term and long-term regions. Two stages of tertiary creep could be distinguished in the slope of the long-term creep curve at 120 MPa, whereas at higher stresses one linear tertiary creep stage is observed (Fig. 4(b)). The rate of acceleration of tertiary creep with time, p, was evaluated as follows [40]:

$$\varepsilon = \varepsilon_0 + \varepsilon_T[1 - \exp(-r' \cdot t)]\dot{\varepsilon}_s t + \varepsilon_3 \cdot \exp[p(t - t_r)], \quad (5)$$

where ε_3 is the tertiary creep strain; this values were obtained graphically from the slope of the $\ln(\Delta/\varepsilon_3)$ vs. $(t - t_t)$ plot, where Δ is the tertiary creep component ($\Delta = \varepsilon - \varepsilon_0 - \varepsilon_T - \dot{\varepsilon}_{min} \cdot t_r$) and t_t is the time to onset of the tertiary stage (Table 3, Fig. 8(a)). In the short-term region, the rate of acceleration of tertiary creep, p, decreases by one order of magnitude with a 20 MPa stress decrease, whereas with transition to long-term region from 140 to 120 MPa it significantly decreases by approximately 2 orders of magnitude (Fig. 8(a)). This finding can be an evidence for the significantly slower recovery processes at low stress.

On the other hand, the decrease in the creep rate with strain at the transient stage is characterized by a $d \ln \dot{\varepsilon}/d\varepsilon$, which is consistent with $\dot{\varepsilon} \sim B \exp(b\varepsilon)$ [11]. The absolute value of this parameter increases from 21 to 75 … 90 with decreasing the applied stress from 180 to 140 …

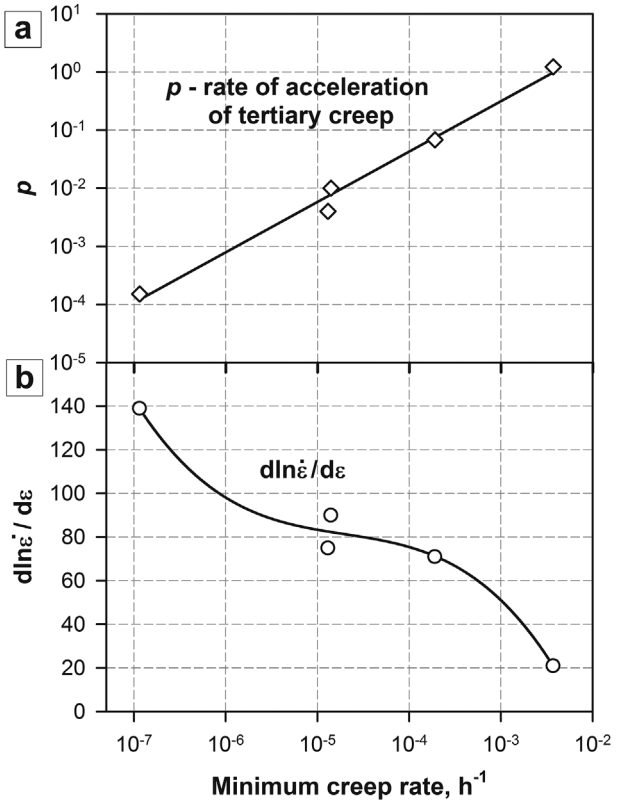

Fig. 8. Change in the parameters of p (a) and $d \ln \dot{\varepsilon}/d\varepsilon$ (b) at tertiary stage with minimum creep rate.

130 MPa and becomes 139 at 120 MPa (Fig. 8(b)). The peculiarity of the tertiary creep at low stress is the presence of two stages distinguished by the $d \ln \dot{\varepsilon}/d\varepsilon$ value. The rapid acceleration of the creep rate occurs in the second stage of tertiary creep, where the $d \ln \dot{\varepsilon}/d\varepsilon$ increases 2.5 times and comprises ~354. This finding is attributed to a void formation starting from the strain of approximately 7% that leads to low ductility (9%) and low reduction in area (22%) (Fig. 3).

3.4. Fracture mode

Fig. 9 shows typical SEM fractographs taken after short-term (a) and long-term (b,c) creep tests. Distinct transgranular fracture in ductile manner occurs during short-term creep (Fig. 9(a)). Dimple rupture results from nucleation of numerous microvoids. Small dimples are approximately 0.5–2.5 μm while coarse dimples are 10–15 μm. Markings of serpentine glide on the walls of coarse dimples evidence for plastic deformation during fracture. In contrast, after long-term creep, the fracture surface has remarkable relief and is affected by oxidation. However, ductile dimple fracture is in dominance, typical dimples are observed (Fig. 9(b)). On the other hand, quasi-cleavage facets and features of intergranular fracture are revealed which can indicate of appearance of ductile fracture component (Fig. 9(c)).

3.5. Changes in TMLS under creep condition

Microstructural changes in the 10% Cr steel were investigated in the creep-ruptured specimens tested at different applied stresses 180, 160, 140 and 120 MPa at 650 °C.

Under short-term creep, the microstructure evolution significantly depends on the applied stress. Thus, the significant plastic flow occurred during creep testing at the highest stress of 180 MPa (t_r = 18.7 h) due to high value of elongation (45%), that led to the slip band formation and bending of boundaries of PAGs and laths

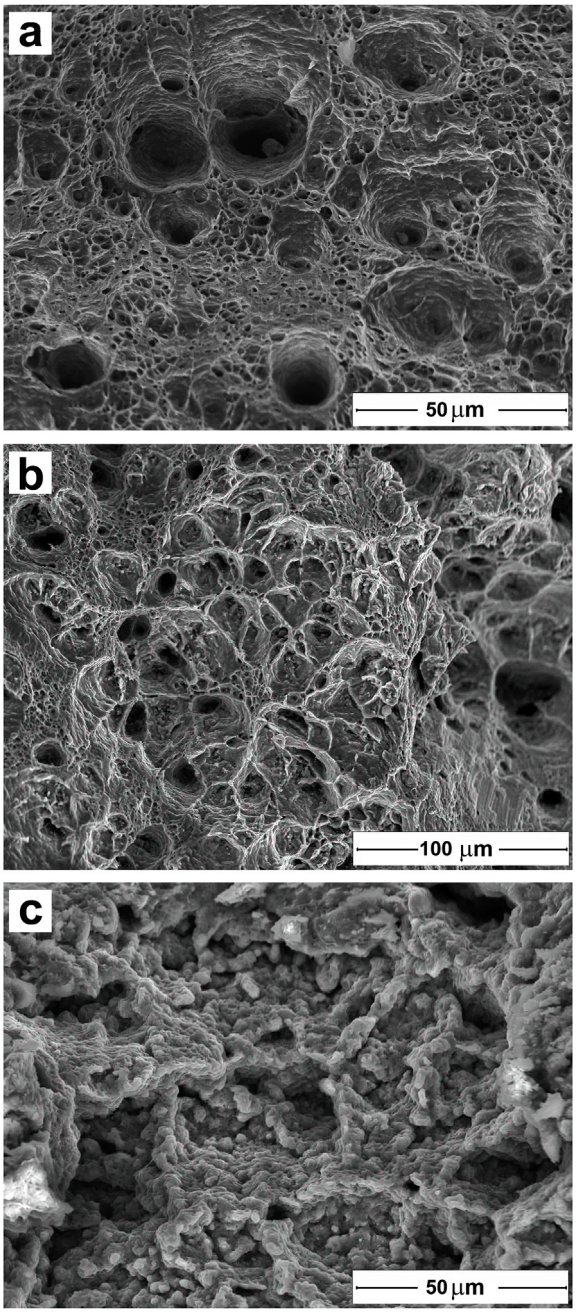

Fig. 9. SEM micrographs of the ruptured surfaces of the 10% Cr steel specimens after (a) short-term (140 MPa, 1426 h) and (b,c) long-term (120 MPa, 39 437 h) creep tests at 650 °C.

(Fig. 10(a)–(c)). Also, the subgrains evolved (Fig. 11(a)). The re-orientation of crystal lattice occurred at high stress that is confirmed by the destruction of "Bain circles" on the {001} pole figures (Fig. 10(a)). A significant decrease in the average KAM value (Fig. 10(b)) was observed, mainly, in the vicinity of LABs and interiors of laths (average KAM is 0.67° in the tempered condition [19]). Nevertheless, the changes in the lath width and dislocation density are insignificant: the lath width increased by 80% and the dislocation density decreased by 30% (Fig. 12(a), Table 1). The partial detachment of the lath boundaries from the chains of boundary precipitates is observed (Fig. 11(a)).

At lower stresses of 160 and 140 MPa (t_r is 211 h and 1426 h, respectively), the lath structure was mostly retained under creep (Fig. 10(d)–(i)). However, the partial destruction of "Bain circles" occurred that is evidence for the re-orientation of the crystal lattice under

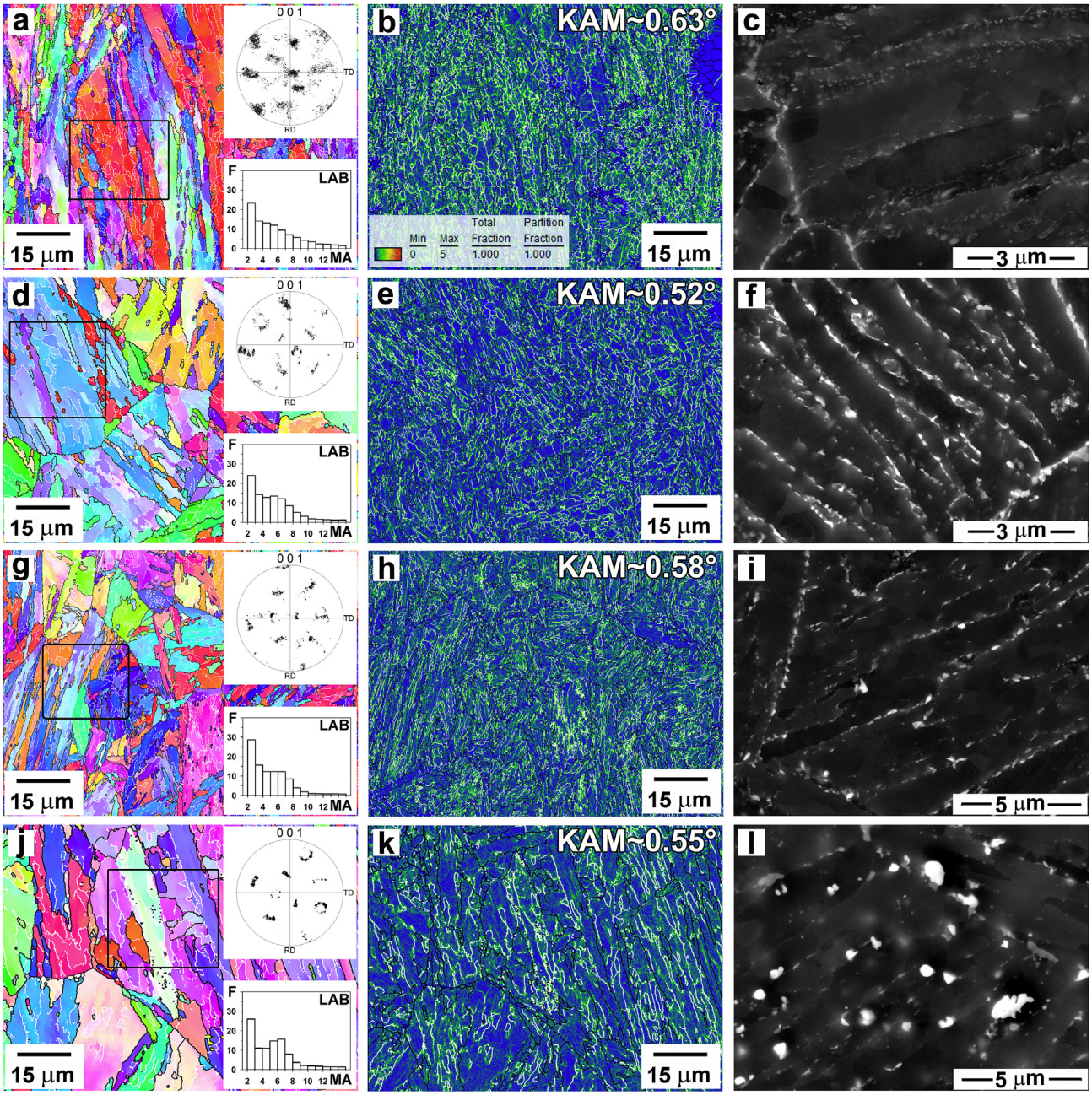

Fig. 10. OIM images with {001} pole figures and distributions of LAB misorientation (a,d,g,j), KAM maps with indicated average KAM values (b,e,h,k) and SEM micrographs (c,f,i,l) of the 10%Cr steel in the gauge section of specimens after creep tests at 650 °C under a stress of: (a,b,c) 180 MPa; (d,e,f) 160 MPa; (g,h,i) 140 MPa; (j,k,l) 120 MPa.

creep (Fig. 10(d) and (g)) [41]. Transformation of some lath boundaries into the subgrain boundaries and their migration leads to the formation of subgrains having elongated shape (Fig. 11(b) and (c)). The lath width increased by 70% while the dislocation density decreased by 70–80%.

Long-term creep at 120 MPa (t_r = 39 437 h) led to a significantly different microstructure (Fig. 10(j–l), 11(d)). Although the duration of creep test was almost 40 000 h, the lath structure was retained until rupture [19]. "Bain circles" are partially destroyed which provides an evidence for the slight re-orientation of the crystal lattice. Approximately 2-fold increase in the lath width leads to an appearance of distinguishable slope of the lath width vs. time to rupture curve (Fig. 12(a)). An increase in the lath width is accompanied by a pronounced (almost one order of magnitude) decrease in the dislocation density (Fig. 12(a)). Two similar stages on the time dependencies of the lath width and dislocation density are observed also after long-term aging (Fig. 12(a)) evidencing for the thermally activated nature of this change.

3.6. Changes in a dispersion of precipitates under creep condition

Dispersion of precipitates is presented in the 10% Cr steel by $M_{23}C_6$ carbides, MX carbonitrides and Laves phase particles both after creep and aging condition.

Laves phase. Precipitation of Laves phase is observed already after 18.7 h of both creep and aging. The precipitated particles have a rather small mean size of about 60 nm and decorate high- and low-angle boundaries (Figs. 10(c) and 11(a)). The mean size of Laves phase particles continuously increases with time to 110–160 nm in the short-term creep region (at 180-140 MPa), whereas long-term creep results in the following 2-fold increase in the mean size to approximately 320 nm

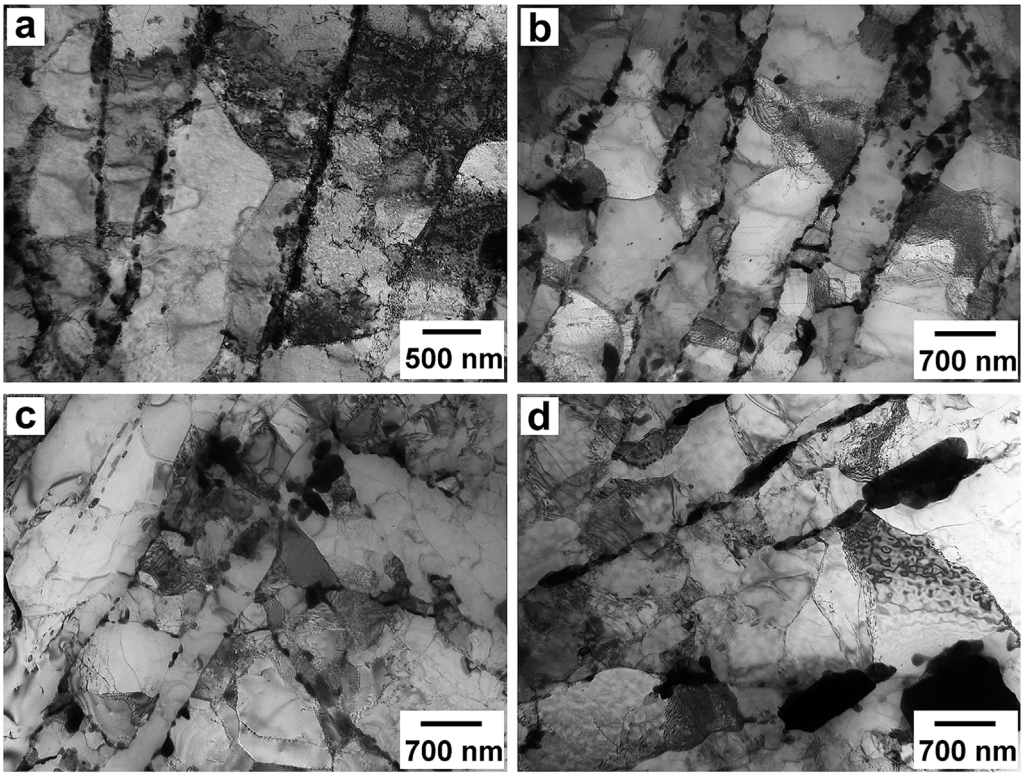

Fig. 11. TEM micrographs of the 10%Cr steel in the gauge section of specimens after creep tests at 650 °C under a stress of: (a) 180 MPa; (b) 160 MPa; (c) 140 MPa; (d) 120 MPa.

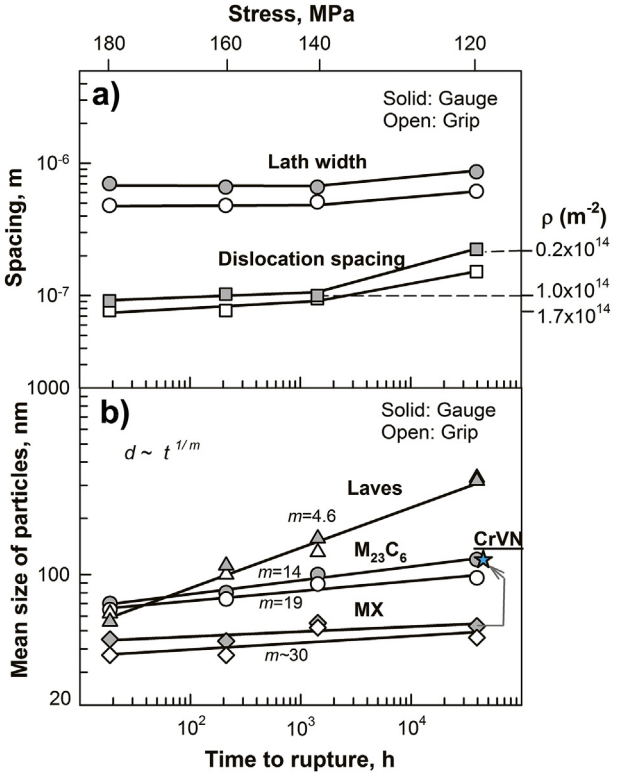

Fig. 12. Change in the parameters of TMLS (a) and mean sizes of particles (b) of the 10%Cr steel under creep (in the gauge sections of specimens, solid symbols) and aging (in the grip sections of specimens, open symbols) conditions at 650 °C and different stresses.

with increasing rupture time from 1426 to 39 437 h (Fig. 12(b)). The size of some large particles reaches about 700–1000 nm (Figs. 11(d) and 13). It was revealed that there is no obvious difference in the size of Laves phase particles after creep and aging, respectively, in the gauge and grip portions (Fig. 12(b)). So, coarsening of Laves phase particles was not strongly affected by strain. Coarsening kinetics is characterized by growth exponent of about 4.6. Previously it was found, that the rapid coarsening of Laves phase occurs during the tertiary stage of long-term creep at 120 MPa [19].

$M_{23}C_6$ carbides. $M_{23}C_6$ carbides located at both LABs and HABs retained their fine dispersion after short-term as well as after long-term creep (Figs. 12(b) and 14, Table 1). The mean size of carbides continuously increases with time (Fig. 12(b)) reaching 120 nm after $\sim 4 \cdot 10^4$ h. The linear time dependencies of the mean $M_{23}C_6$ size are observed with the similar growth exponent of 14 for the creep and 19 for aging conditions. So, a strain-induced coarsening of $M_{23}C_6$ carbides is slightly faster in comparison with aging. Only in the long-term creep region, a slight difference of approximately 50 nm appears between the peak sizes in the grip and gauge sections of specimens (Fig. 14(d)). In contrast, in the short-term region the distributions of $M_{23}C_6$ carbide size are the same (Fig. 14(a–c)). As it was shown in Ref. [19], a significant part of carbide coarsening occurred during the secondary part of tertiary stage under long-term creep. The values of growth exponent for $M_{23}C_6$ carbides are about 4 times lower than for Laves phase particles.

MX carbonitrides. In the short-term region, homogeneously distributed MX carbonitrides are represented mainly by Nb-rich M(C,N) particles, whereas V-rich particles were not revealed in the crept specimens. Nb-rich carbonitrides exhibit the slowest growth kinetics with the growth exponent of about 30 (Fig. 12(b)). During long-term creep and aging, V-rich carbonitrides precipitate. These particles appear between 1000 and 10 000 h of creep/aging and then slightly grow reaching 67 and 58 nm after long-term creep and aging for approximately 40 000 h, respectively [19]. Strain-induced transformation of a part of V-rich carbonitrides into Z-phase occurs in tertiary stage of

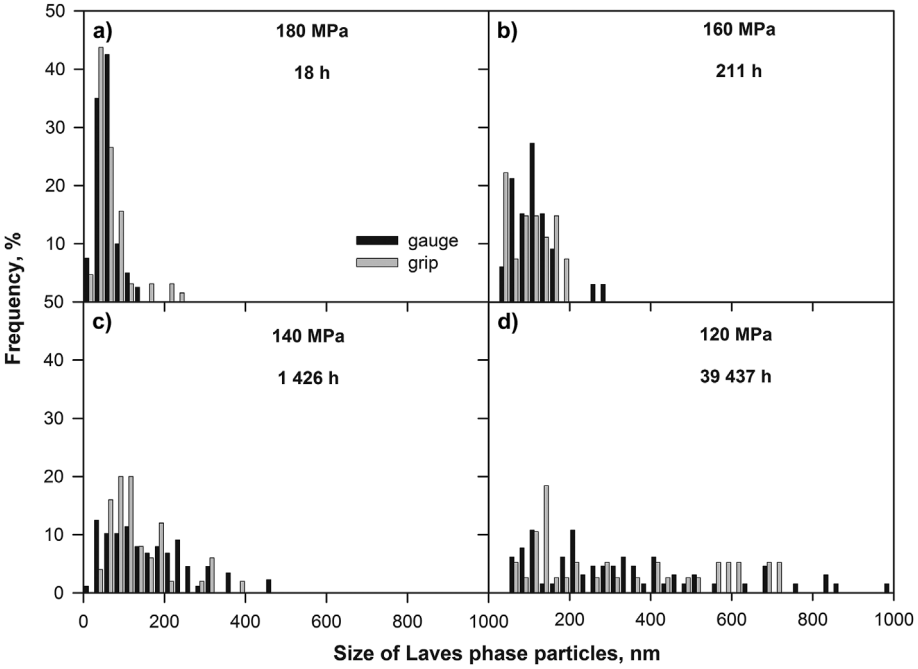

Fig. 13. Size distributions of the Laves phase particles in the 10%Cr steel after creep at 650 °C under a stress of: a) 180 MPa; b) 160 MPa; c) 140 MPa; d) 120 MPa.

creep. However, Z-phase particles have rather small size of 120 nm due to low N content.

Therefore, the slight increase in the lath width and dislocation density in the short-term creep region is accompanied by the insignificant increase in the mean size of $M_{23}C_6$ carbides and MX carbonitrides and coarsening of precipitated Laves phase particles to approximately 160 nm. On the other hand, the more pronounced lath widening and decrease in the dislocation density is attributed to significant coarsening of Laves phase particles during long-term creep.

4. Discussion

4.1. Creep behavior

As it was shown in Section 3.3, the stress exponent tends to increase with decreasing the stress that can be indicative of the presence of threshold stress in the 10%Cr steel studied [42]. Under an applied stress less than the threshold stress either the creep processes do not occur or the creep rate is negligibly low [34,35]. Therefore, the creep behavior is represented by the following relationship [34]:

$$\dot{\varepsilon}_{\min} = A(\sigma - \sigma_{th})^n \quad (6)$$

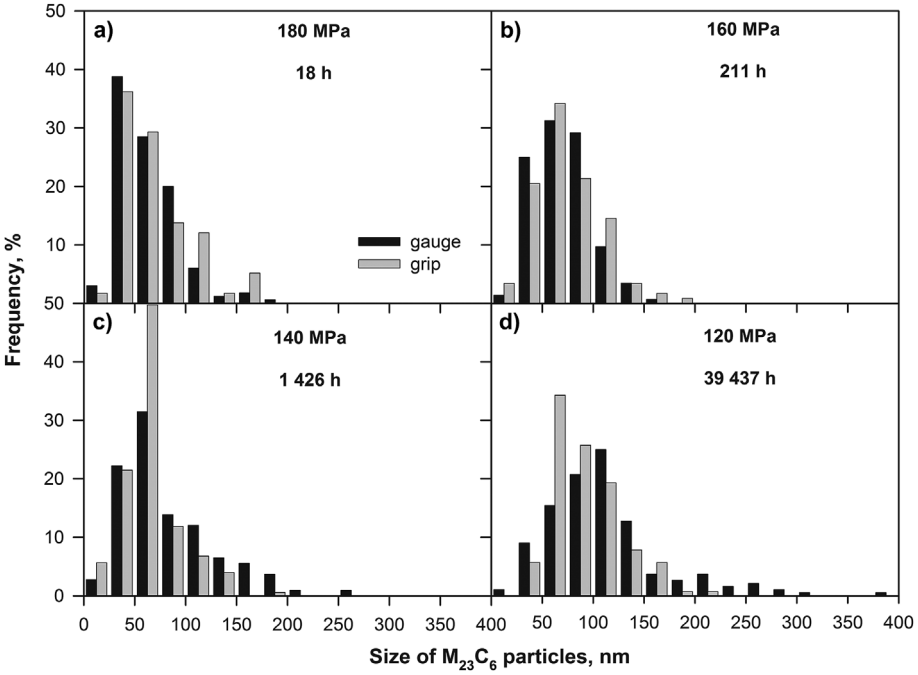

Fig. 14. Size distributions of the $M_{23}C_6$ carbides in the 10%Cr steel after creep at 650 °C under a stress of: a) 180 MPa; b) 160 MPa; c) 140 MPa; d) 120 MPa.

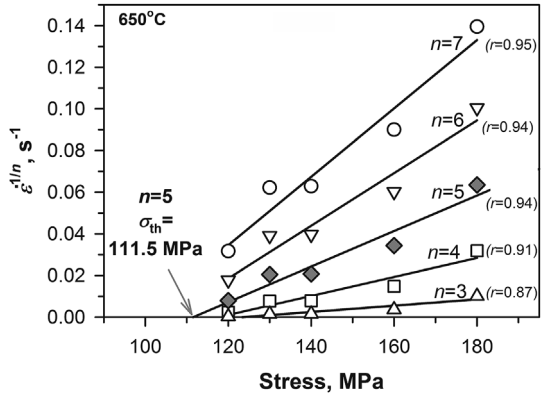

Fig. 15. $\dot{\varepsilon}^{1/n} - \sigma$curves of the 10%Cr steel for temperature of 650 °C. Linear approximation for determining the threshold stresses: $n = 3$ and 4 - the regression coefficient is low; starting from $n = 5$, points fit a straight line with regression coefficient of 0.94–0.95.

where σ_{th} is the threshold stress, n is the true stress exponent. Estimation of the threshold stress by the following technique [43,44] revealed that the true stress exponent n is 5 since this value yields the best linear fit of experimental data plotted as $\dot{\varepsilon}_{min}^{1/n}$ against the stress, σ, on double-linear scale (Fig. 15). Extrapolating this straight line to a zero creep rate yields a threshold stress of 111.5 MPa. It should be noted that this value matches well with the value of ~110 MPa obtained from extrapolating the curve on Fig. 6 at a creep rate of 10^{-11} s^{-1}. As it was shown in Ref. [45], this simple procedure also can be used for estimating the threshold stresses. The value $n = 5$ in power law estimated using threshold stress concept is in accordance with the data obtained for the 9%Cr steels [20,46]. The threshold stress of 111.5 MPa in the 10% Cr steel is high and about 30% larger than that in the P92-type steel [12,20,36].

Fig. 16 shows the dependence of creep rate on the effective stress (σ-σ_{th}). Normalized creep rate $\dot{\varepsilon}kT/DGb$versus the normalized effective stress $(\sigma - \sigma_{th})/G$ is also shown on Fig. 16 accordingly to relationship

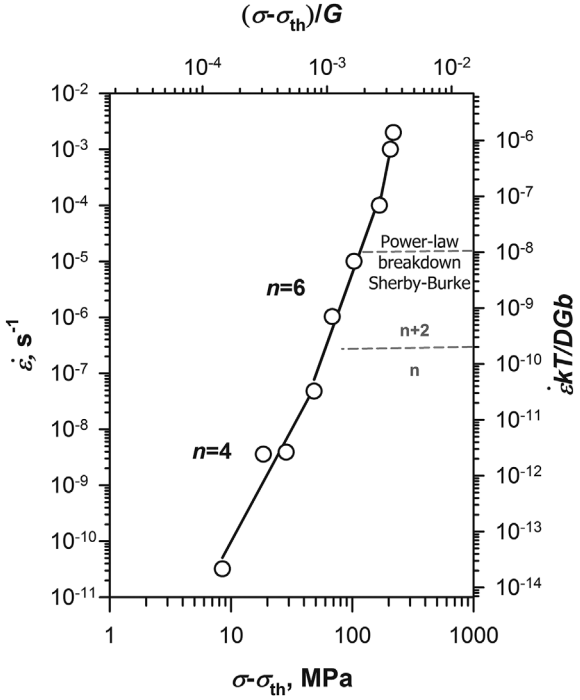

Fig. 16. Creep rate/or normalized creep rate vs. effective stress/or normalized effective stress for the 10%Cr steel at 650 °C.

[45]:

$$\dot{\varepsilon} = \frac{ADGb}{kT}\left(\frac{\sigma - \sigma_{th}}{G}\right)^n \quad (7)$$

where D is the appropriate diffusion coefficient and estimated as $D = D_o\exp(-Q/RT)$ [35,47], where Do is a frequency factor, G is the shear modulus, Q is the activation energy, R is the gas constant, T is the absolute temperature, k is the Boltzmann's constant. The following parameters were used for the calculations: $G = 60$ GPa at 650 °C [48]; $b = 2.48{\cdot}10^{-10}$ m; $D_o = 2{\cdot}10^{-4}$ m^2/s; activation energy for lattice diffusion $Q = 251$ kJ/mol [35].

Two regions of power-law creep of the 10%Cr steel at 650 °C can be distinguished with different slope which is the true stress exponent n. At low creep rates, the power law with stress exponent n~4 occurs, whereas at higher creep rates the true stress exponent n~6. An inflection point between two regions occurs at normalized creep rate of $\dot{\varepsilon}kT/DGb$~10^{-10} (or creep rate of ~10^{-7} s^{-1}) and normalized effective stress $(\sigma - \sigma_{th})/G$~10^{-3} (or $(\sigma$-$\sigma_{th}) \sim 60$ MPa).

Creep processes in the power-law creep region are controlled by dislocation climb [35,47]. The classical change in stress exponent $n = n + 2$ with transition from low-creep rate/or high-temperature region to high-creep rate/or low-temperature region is observed that is attributed to change in the mechanism controlling the rate of dislocation climb. Usually, the slowest controlling mechanism changes from lattice diffusion to grain-boundary or pipe diffusion [35,47]. Accordingly to criterion established by Sherby and Burke [49] the power-law breakdown occurs at normalized creep rate of 10^{-8}. So, a creep behavior at 650 °C and applied stresses > ~200 MPa is characterized as exponential creep.

Therefore, at 650 °C, creep behavior of the 10%Cr steel under applied stress ranging from 120 … 160 MPa is characterized as high-temperature power-law creep controlled by dislocation climb. At higher stresses, approximately 160 … 200 MPa, the low-temperature creep occurs. So, the creep at 120 MPa as well as 140 MPa belongs to the power-law creep region. This finding is in accordance with the results on the P91-type steel [50,51] which demonstrates the transition from power-law to viscous creep at stresses less than 100 MPa at 923 K. Nevertheless, the applied stress of 120 MPa is very close to the threshold stress value (111.5 MPa) that can explain the significant decrease in the creep rate and rise in the long-term creep strength of the 10%Cr steel.

4.2. Origin of threshold stress

The threshold stress can be associated with a dispersion of precipitates acting as the effective barriers to mobile dislocations. Fine particles which are homogeneously distributed in the lath interiors seem to be the most effective barriers. In the 10% Cr steel studied, MX carbonitrides locate in the lath interiors, while $M_{23}C_6$ carbides and Laves phase particles are situated on the grain/lath boundaries (Fig. 17).

According to different models [34,42,52,53] the threshold stress can be attributed to the stress required to:

- bow a dislocation between two particles (Orowan stress);
- generate the additional length of dislocation to climb over an obstacle (climb stress);
- detach the dislocation from an attractive particle after finishing the climb (detachment stress).

Orowan stress, τ_O, can be evaluated as [42]:

$$\tau_O = 0.84\,Gb\,/\,(\lambda - d) \quad (8)$$

where G is the shear modulus, b is the Burger's vector, d is the particle size, and λ is the antiparticles distance, which is estimated as [54]:

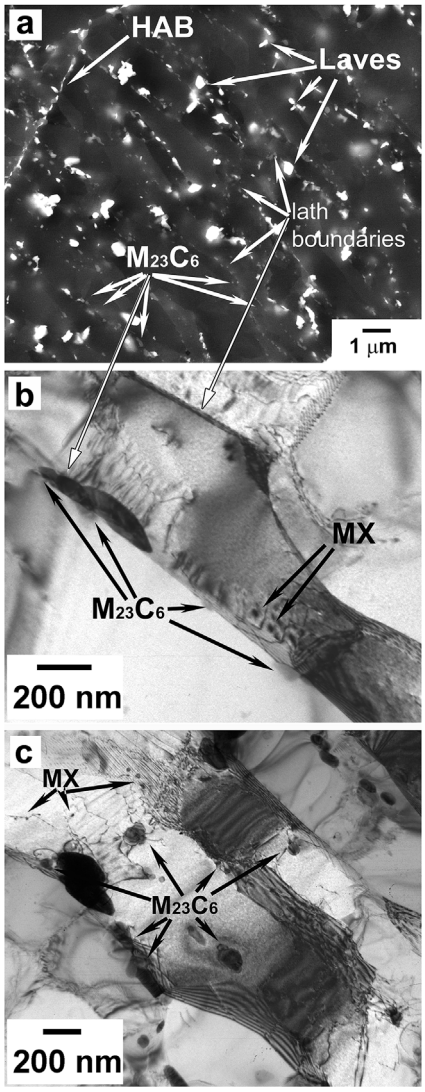

Fig. 17. Dispersion of particles in the 10% Cr steel at the apparent steady-state creep stage at 650 °C and 120 MPa, 10 000 h: a) SEM, b, c) TEM micrographs show interaction between fine $M_{23}C_6$ and MX precipitates and dislocations.

$$\lambda = 0.5d\sqrt{\pi/6F_v} \tag{9}$$

where F_v is the volume fraction of the particles.

The climb stress, τ_c, can be derived from the equation [42,52]:

$$\tau_c = 0.3\,Gb\,/\,\lambda \tag{10}$$

The detachment stress, τ_d, can be calculated from the equation [42,52,53]:

$$\tau_d = Gb\sqrt{1-K^2}/\lambda \tag{11}$$

where K is the relaxation parameter.

The values of different types of stresses (Orowan stress, the climb stress and detachment stress) exerted by MX carbonitrides were estimated in the 10% Cr steel at 650 °C at the minimum creep rate stage under an applied stress of 140 MPa and 120 MPa. These two points correspond to 780 and 10 000 h of creep test, respectively [14,19]. The following parameters were used for the calculations: $G = 60$ GPa at 650 °C [48]; $b = 2.48{\cdot}10^{-10}$ m; the mean size d and volume fraction of particles F_v (as estimated by Thermo-Calc) are presented in Table 4. It should be noted that at the 120 MPa the volume fraction of MX phase is about 25% larger due to precipitation of V-rich MX carbonitrides during the transient creep stage [19]. A relaxation parameter was assumed to be 0.7 [52,53]. The values of estimated stresses together with the value of the threshold shear stress, τ_{th}, (which is $\sigma_{th}/2 = 55.75$ MPa) are presented in Table 4 and Fig. 18.

The threshold stress can not be associated with MX particles only, because the values of Orowan stress, the climb stress and detachment stress exerted by MX carbonitrides are significantly lower than the threshold shear stress of 55.75 MPa. This finding is probably attributed to low fraction of MX phase in the 10% Cr steel due to low N content. At the same time the value of the detachment stress exerted by $M_{23}C_6$ carbides is close to the level of the threshold shear stress (Table 4, Fig. 18).

The summarizing of the detachment stresses from MX carbonitrides, $M_{23}C_6$ carbides, and Laves phase particles as the superposition of these stresses $\Sigma\tau_d = \sqrt{\tau^2_{d(MX)} + \tau^2_{d(M23C6)} + \tau^2_{d(Laves)}}$ leads to the value of total detachment stress $\Sigma\tau_d = 55.9$ MPa (at 120 MPa) that is close to the threshold shear stress (Fig. 18, Table 4).

It is interesting to note, that precipitation of V-rich MX carbonitrides during long-term transient stage of creep testing at 120 MPa leads to an increase in the stress from MX carbonitrides by 40% as compared with that at short-term creep at 140 MPa (Table 4). On the other hand, the coarsening of Laves phase particles results in a decrease in the stress from Laves phase at 120 MPa.

So, in the apparent steady-state stage of creep, the essentially stable $M_{23}C_6$ carbides evidently exert the main part of threshold stress in the 10% Cr steel. As it was found [19], these carbides retain their nanoscale size up to 100 nm during ~$4{\cdot}10^4$ h of aging at 650 °C and ~1 … $3{\cdot}10^4$ h of long-term creep at 120 MPa.

For the P92-type steel with standard volume fraction of MX phase of 0.23%, it was revealed that the shear threshold stress of approximately 50 MPa at 650 °C is attributed to stress from MX dispersoids [20,55]. The stress for detachment of lattice dislocations from MX carbonitrides was close to threshold stress and comprised approximately 51 MPa. In contrast, in the 10% Cr steel the approximately 5 times lower fraction of MX particles (0.044%) results in approximately 3 times lower the stress exerted from MX particles as compared with the P92 steel [20,49]. Nevertheless, in the 10% Cr steel even at the absence of high fraction of MX phase the stable $M_{23}C_6$ carbides are able to provide the high threshold stress. The minimal creep rate of the 10% Cr steel is approximately 2 orders of magnitude lower than that of the P92 steel.

4.3. Evolution of pinning pressures at tertiary creep

To reveal the role of precipitates in the microstructure evolution at tertiary creep the analysis of the pinning of (sub)grain/lath boundaries by various secondary-phase particles was carried out. The pinning pressures on the grain/subgrain boundaries from different precipitates were estimated using a technique described in Refs. [13,56,57].

Homogeneously distributed precipitates exert Zener pinning pressure on a boundary, which can be estimated as follows [13,54,56,57]:

$$P_Z = \frac{3\gamma F_V}{d} \tag{12}$$

where γ is the boundary surface energy per unit area, and F_v and d are the volume fraction and size of dispersed particles, respectively. When particles are located on boundaries, the pinning pressure on a boundary depends on the size ratio of particles and subgrains/laths [58], and can be evaluated as follows:

$$P_B = \frac{\gamma F_{vB} D}{d^2} \tag{13}$$

where $F_{vB}$is the volume fraction of the particles located at the boundaries, and D is the size of structural elements, i.e. the subgrain size or lath thickness. F_{vB} was estimated as presented in Ref. [13]. The densities of boundary $M_{23}C_6$ and Laves phase particles, which were calculated under the assumption that all $M_{23}C_6$ and Laves phase particles are located at lath and (sub)grain boundaries were taken into account

Table 4
Parameters of second phases and estimated values of Orowan stress, the climb stress, the detachment stress in the 10%Cr steel.

	Mean size of particles, d (nm)/Volume fraction, Fv		Orowan stress (τ_0) MPa		Climb stress (τ_c) MPa		Detachment stress (τ_d), MPa	
	140 MPa, 780 h	120 MPa, 10000 h	140 MPa	120 MPa	140 MPa	120 MPa	140 MPa	120 MPa
$M_{23}C_6$	88/0.0213	85/0.0213	96	99.4	20.5	21.2	48.7	50.4
Laves	157/0.0183	222/0.0183	47.6	33.6	10.6	7.5	25.3	17.9
Nb-rich MX	48/0.000354	36/0.000354	14.3	19.1	4.8	6.5	11.5	15.4
V-rich MX	−/−	60/0.0000862	0	5.5	0	1.9	0	4.6
$\Sigma\tau_{(all\ particles)}$			108.1	106.8	23.6	23.5	56.1	55.9
$\Sigma\tau_{(MX)}$			14.3	19.8	4.8	6.7	11.5	16.06

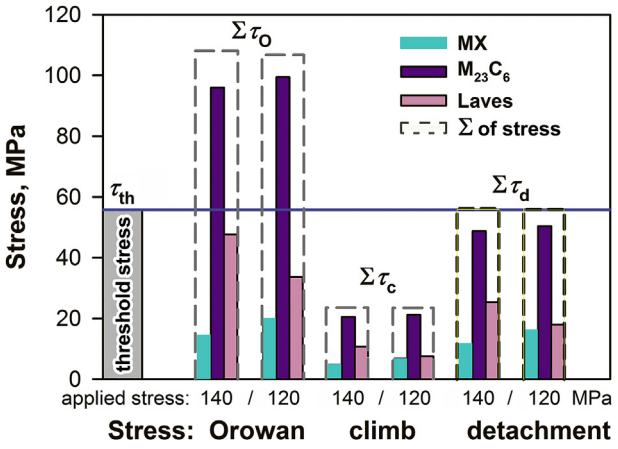

Fig. 18. Orowan stress, the climb stress and detachment stress, estimated for MX, $M_{23}C_6$ and Laves phase particles in the 10%Cr steel at the apparent steady-state creep stage during short-term (140 MPa, 780 h) and long-term (120 MPa, 10 000 h) creep tests at 650 °C. Blue horizontal line shows the level of threshold shear stress; dotted lines show the total stress from all types of particles. (For interpretation of the references to colour in this figure legend, the reader is referred to the Web version of this article.)

calculating Zener drag exerted by $M_{23}C_6$ and Laves phase particles.

Fig. 19 presents the change in the pinning pressures with creep time. $M_{23}C_6$ carbides exert the highest pinning pressure as compared to other

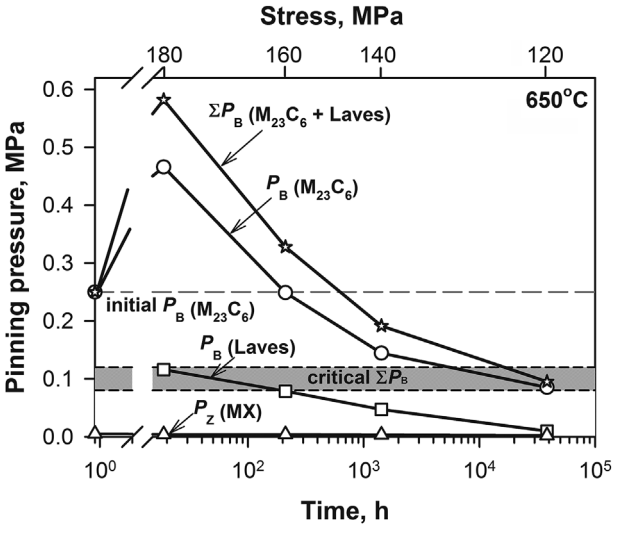

Fig. 19. Change in the pinning pressure from $M_{23}C_6$ carbides and Laves phase particles in the gauge portion on the grain and lath boundaries of the 10% Cr steel during creep tests at 650 °C and different applied stresses 180-120 MPa. The dotted line indicates the level of pinning pressure from $M_{23}C_6$ carbides in the tempered state. Interval of critical values of pinning pressure corresponds to Ref. [13].

precipitates. In the short-term region, the pinning pressure continuously decreases with time. At the long-term creep, the summary pinning pressure from carbides and Laves phase reaches the lower boundary of critical interval reported in Ref. [13].

Therefore, this can explain why this long-term creep point still keeps the linear character of the stress vs. time dependence and creep strength degradation does not occur. It can be suggested that this point (120 MPa) could be the transition point followed by strength breakdown at more than 40 000 h. The critical factors affecting this degradation could be named as following.

1) Coarsening of Laves phase particles. It is evident that this coarsening is not strain-induced and depends on exposition time. During 40 000 h of both aging and creep, coarsening of Laves phase is significant. On the other hand, the coarsening rate of Laves phase is about two times lower in comparison with the 9%Cr steel with the same content of W and B as in the 10% Cr steel studied [59]. Since the coarsening rate of Laves phase depends on chemical composition of steel, the chemical and microstructural design of the 10% Cr steel studied proves to be effective in an increasing the coarsening resistance of Laves phase particles too.
2) The growth of Laves phase, in its turn, leads to the continuous coarsening of carbides. As far as $M_{23}C_6$ carbides demonstrate the stable nanoscale size until approximately 20 000 h during creep (at 120 MPa, for example), carbides may be predicted to be effective in the case if the time duration of the apparent steady-state stage will last up to 40 000 h testing (under lower stress).
3) Coarsening of Z-phase particles. The longer time can lead to an increase in the volume fraction and coarsening of Z-phase that will negatively affect the creep resistance [23].

5. Conclusions

The creep behavior at 650 °C and changes in microstructure and precipitations of secondary phases were studied in advanced 10% Cr martensitic steel with 0.008% B and 0.003% N. The main results can be summarized as follows:

1. The 100 000 h (650 °C) creep rupture strength is predicted to be 110 MPa. The stress vs. time to rupture dependence does not demonstrate creep strength breakdown up to approximately 40 000 h. Short-term and long-term creep regions are distinguished at 180-140 MPa and at ≤ 120 MPa, respectively.
2. Monkman-Grant diagram is linear and characterized by values of $c' = 0.225$ and $m' = 0.74$ in the relation $t_r = (c'/\dot{\varepsilon}_{min})^{m'}$.
3. Tempered martensite lath structure does not transform to subgrain structure under short-term and long-term creep conditions. Coarsening of lath structure during long-term creep is associated with coarsening of Laves phase particles, mainly.
4. Analysis in terms of threshold stress reveals the value of threshold stress of 111.5 MPa. At 650 °C, creep of the 10%Cr steel under a stress ranging from 120 … 160 MPa is characterized as high-temperature power-law creep with stress exponent $n \sim 4$, while the low-

temperature creep occurs with $n \sim 6$ at higher stress 160 … 180 MPa.

5. Threshold stress is associated with the detachment stress, i.e. the stress required for detachment of dislocations from $M_{23}C_6$ carbides after finishing the climb, mainly. MX carbonitrides induce the significantly lower detachment stress.

Acknowledgments

The study was financial supported by the Ministry of Education and Science of Russian Federation, Russian Federation, project of Government Task No. 11.2868.2017/PCh (number for publication 11.2868.2017/4.6). The authors are grateful to the staff of the Joint Research Center, «Technology and Materials», Belgorod State University, for providing the equipment for instrumental analysis.

References

[1] F. Abe, T.-U. Kern, R. Viswanathan, Creep-Resistant Steels, Woodhead Publishing, Cambridge, 2008.
[2] R.O. Kaybyshev, V.N. Skorobogatykh, I.A. Shchenkova, New martensitic steels for fossil power plant: creep resistance, Phys. Met. Metallogr. 109 (2010) 186–200.
[3] F. Abe, Research and development of heat-resistant materials for advanced USC power plants with steam temperatures of 700°C and above, Engineering 1 (2) (2015) 211–224.
[4] X. Xie, Y. Wu, C. Chi, M. Zhang, Superalloys for Advanced Ultra-super-critical Fossil Power Plant Application, (2015), https://doi.org/10.5772/61139.
[5] K. Maruyama, K. Sawada, J. Koike, Strengthening mechanisms of creep resistant tempered martensitic steel, ISIJ Int. 41 (2001) 641–653.
[6] A. Kostka, K.-G. Tak, R.J. Hellmig, Y. Estrin, G. Eggeler, On the contribution of carbides and micrograin boundaries to the creep strength of tempered martensite ferritic steels, Acta Mater. 55 (2007) 539–550.
[7] A. Aghajani, Ch Somsen, G. Eggeler, On the effect of long-term creep on the microstructure of a 12% chromium tempered martensite ferritic steel, Acta Mater. 57 (2009) 5093–5106.
[8] K. Kimura, H. Kushima, K. Sawada, Long-term creep deformation property of modified 9Cr–1Mo steel, Mater. Sci. Eng. A 510–511 (2009) 58–63.
[9] M. Yoshizawa, M. Igarashi, K. Moriguchi, A. Iseda, H.G. Armaki, K. Maruyama, Effect of precipitates on long-term creep deformation properties of P92 and P122 type advanced ferritic steels for USC power plants, Mater. Sci. Eng. A 510–511 (2009) 162–168.
[10] H.G. Armaki, R. Chen, K. Maruyama, M. Igarashi, Contribution of recovery mechanisms of microstructure during long-term creep of Gr.91steels, J. Nucl. Mater. 433 (2013) 23–29.
[11] F. Abe, Creep behavior, deformation mechanisms and creep life of mod.9Cr-1Mo steel, Metall. Mater. Trans. A 46 (2015) 5610–5625.
[12] V.A. Dudko, A.N. Belyakov, R.O. Kaibyshev, Sources of high creep resistance of modern high-chromium martensitic steels, Dokl. Phys. Chem. 464 (2015) 191–193.
[13] A. Fedoseeva, N. Dudova, R. Kaibyshev, Creep strength breakdown and microstructure evolution in a 3%Co modified P92 steel, Mater. Sci. Eng. A 654 (2016) 1–12.
[14] R. Mishnev, N. Dudova, R. Kaibyshev, Microstructural aspects of superior creep resistance of a 10%Cr martensitic steel, Mater. Sci. Eng. A 678 (2016) 178–189.
[15] J. Haid, S. Straub, V. Foldyna, Microstructural stability of 9 - 12%CrMo(W)VNbN-steels, Materials for Advanced Power Engineering, Forschungszentrum Jülich GmbH, 1998, pp. 155–170.
[16] R. Ishii, Y. Tsuda, K. Kimura, M. Yamada, Change of microstructure during high temperature exposure of 1 OCr-lMo-1 W—VNbN steel, CAMP –ISIJ 12 (1999) 441.
[17] Y. Shen, H. Liu, Zh Shang, Zh Xu, Precipitate phases in normalized and tempered ferritic/martensitic steel P92, J. Nucl. Mater. 465 (2015) 373–382.
[18] I. Fedorova, A. Kostka, E. Tkachev, A. Belyakov, R. Kaibyshev, Tempering behavior of a low-nitrogen boron-added 9%Cr steel, Mater. Sci. Eng. A 662 (2016) 443–455.
[19] R. Mishnev, N. Dudova, R. Kaibyshev, On the origin of the superior long-term creep resistance of a 10% Cr steel, Mater. Sci. Eng. A 713 (2018) 161–173.
[20] V. Dudko, A. Belykov, R. Kaibyshev, Evolution of lath substructure and internal stresses in a 9% Cr steel during creep, ISIJ Int. 57 (2017) 540–549.
[21] M. Mitsuhara, Sh Yamasaki, M. Miake, H. Nakashima, M. Nishida, J. Kusumoto, A. Kanaya, Creep strengthening by lath boundaries in 9Cr ferritic heat resistant steel, Philos. Mag. Lett. 96 (2016) 76–83.
[22] H. Semba, F. Abe, Alloy design and creep strength of advanced 9%Cr USC boiler steels containing high concentration of boron, Energy Mater. 1 (2006) 238–244.
[23] J. Hald, Microstructure and long-term creep properties of 9-12% Cr steels, Int. J. Press. Vessel. Pip. 85 (2008) 30–37.
[24] F. Abe, Effect of boron on microstructure and creep strength of advanced ferritic power plant steels, Procedia Eng. 10 (2011) 94–99.
[25] N. Dudova, R. Kaibyshev, On the precipitation sequence in a 10%Cr Steel under tempering, ISIJ Int. 51 (2011) 826–831.
[26] R. Sahara, T. Matsunaga, H. Hongo, M. Tabuchi, Theoretical investigation of stabilizing mechanism by boron in body-centered cubic iron through $(Fe,Cr)_{23}(C,B)_6$ precipitates, Metall. Mater. Trans. A 47 (2016) 1–11.
[27] I. Fedorova, F. Liu, F.B. Grumsen, Y. Cao, O.V. Mishin, J. Hald, Fine $(Cr,Fe)_2B$ borides on grain boundaries in a 10Cr-0.01B martensitic steel, Scr. Mater. 156 (2018) 124–128.
[28] R. Mishnev, N. Dudova, V. Dudko, R. Kaibyshev, Impact toughness of a 10% Cr steel with high boron and low nitrogen contents, Mater. Sci. Eng. A 730 (2018) 1–9.
[29] B. Wilshire, P. Scharning, Prediction of long term creep data for forged 1Cr-1Mo-0.25V steel, Mater. Sci. Technol. 24 (2008) 1–9.
[30] K. Haarmann, J.C. Vaillant, B. Vandenberghe, W. Bendick, A. Arbab, The T91/P91 Book, Vallourec and Mannesmann Tubes, Boulogne, 2002.
[31] A. Fedoseeva, N. Dudova, R. Kaibyshev, A. Belyakov, Effect of tungsten on creep behavior of 9%Cr-3%Co martensitic steels, Metals 7 (12) (2017), https://doi.org/10.3390/met7120573 No. 573.
[32] F. Garofalo, Fundamentals of Creep and Creep Rupture in Metals, MacMillan, New York, NY, 1965.
[33] J. Vanaja, K. Laha, M.D. Mathew, Effect of tungsten on primary creep deformation and minimum creep rate of reduced activation ferritic-martensitic steel, Metall. Mater. Trans. A 45 (2014) 5076–5084.
[34] M.E. Kassner, M.T. Pérez-Prado, Fundamentals of Creep in Metals and Alloys, first ed., Elsevier, Amsterdam, Boston, 2004, p. 272.
[35] H. Frost, M. Ashby, Deformation Mechanism Maps, Pergamon Press, Oxford, New York, 1982, p. 166.
[36] T. Sakthivel, S. Panneer Selvi, K. Laha, An assessment of creep deformation and rupture behaviour of 9Cr–1.8W–0.5Mo–VNb (ASME grade 92) steel, Mater. Sci. Eng. A 640 (2015) 61–71.
[37] K. Kimura, Y. Toda, H. Kushima, K. Sawada, Creep strength of high chromium steel with ferrite matrix, Int. J. Press. Vessel. Pip. 87 (6) (2010) 282–288.
[38] E. Isaac Samuel, B.K. Choudhary, D.P. Rao Palaparti, M.D. Mathew, Creep deformation and rupture behaviour of P92 steel at 923 K, Procedia Eng. 55 (2013) 64–69.
[39] F.C. Monkman, N.J. Grant, Proc. ASTM 56 (1956) 593–620.
[40] J. Vanaja, K. Laha, Assessment of tungsten content on tertiary creep deformation behavior of reduced activation ferritic-martensitic steel, Metall. Mater. Trans. A 46 (2015) 4669–4679.
[41] R.K. Ray, J.J. Jonas, Transformation textures in steels, Int. Mater. Rev. 35 (1) (1990) 1–36.
[42] F.A. Mohamed, K.-T. Park, E.J. Lavernia, Creep behavior of discontinuous SiCAl composites, Mater. Sci. Eng. A 150 (1992) 21–35.
[43] W.C. Oliver, W.D. Nix, High temperature deformation of oxide dispersion strengthened Al and Al-Mg solid solutions, Acta Metall. 30 (1982) 1335–1347.
[44] R. Kaibyshev, O. Sitdikov, I. Mazurina, Deformation behavior of a 2219 Al alloy, Mater. Sci. Eng. 334 (2002) 104–113.
[45] Y. Li, T.G. Langdon, A simple procedure for estimating threshold stresses in the creep of metal matrix composites, Scr. Mater. 36 (1997) 1457–1460.
[46] S. Spigarelli, E. Cerri, P. Bianchi, E. Evangelista, Interpretation of creep behavior of a 9Cr-Mo-Nb-V-N (T91) steel using threshold stress concept, Mater. Sci. Technol. 15 (1999) 1433–1440.
[47] S.V. Raj, T.G. Langdon, Creep behavior of copper at intermediate temperatures – I. Mechanical characteristics, Acta Metall. 37 (1989) 843–852.
[48] J. Cadek, V. Sustek, M. Pahutova, An analysis of a set of creep data for a 9Cr-1Mo-0.2V (P91 type) steel, Mater. Sci. Eng. A 225 (1997) 22–28.
[49] O.D. Sherby, P.M. Burke, Mechanical behavior of crystalline solids at elevated temperature, Prog. Mater. Sci. 13 (1968) 323–390, https://doi.org/10.1016/0079-6425(68)90024-8.
[50] L. Kloc, V. Sklenicka, Transition from power-law to viscous creep behavior of P-91 type heat-resistant steel, Mater. Sci. Eng. A 234–236 (1997) 962–965.
[51] V. Sklenicka, K. Kucharova, M. Svoboda, L. Kloc, J. Bursik, A. Kroupa, Long-term creep behavior of 9-12%Cr power plant steels, Mater. Char. 51 (2003) 35–48.
[52] E. Arzt, D. Wilkinson, Threshold stresses for dislocation climb over hard particles: the effect of an attractive interaction, Acta Metall. 34 (1986) 1893–1898.
[53] J. Rosler, E. Arzt, A new model-based creep equation for dispersion strengthened materials, Acta Metall. Mater. 38 (1990) 671–683.
[54] F.J. Humphreys, M. Hatherly, Recrystallization, Related Annealing Phenomena, second ed., Elsevier, Oxford, 2004.
[55] V. Dudko, A. Belyakov, R. Kaibyshev, Origin of threshold stresses in a P92-type steel, Trans. Indian Inst. Met. 69 (2016) 223–227.
[56] N. Dudova, A. Plotnikova, D. Molodov, A. Belyakov, R. Kaibyshev, Structural changes of tempered martensitic 9%Cr–2%W–3%Co steel during creep at 650 °C, Mater. Sci. Eng. A 534 (2012) 632–639.
[57] A. Fedoseeva, N. Dudova, R. Kaibyshev, Creep behavior and microstructure of a 9Cr–3Co–3W martensitic steel, J. Mater. Sci. 52 (2017) 2974–2988.
[58] W.B. Hutchinson, B.J. Duggan, Influence of precipitation on recrystallization and texture development in an iron-1.2% copper alloy, Met. Sci. 12 (1978) 372–380.
[59] E. Tkachev, A. Belyakov, R. Kaibyshev, Creep behavior and microstructural evolution of a 9%Cr steel with high B and low N contents, Mater. Sci. Eng. A 725 (2018) 228–241.